Fiber Bragg Grating-based sensor system for sensing the shape of flexible needles

Leifeng Zhang [a], Changle Li [a], Huijuan Dong [a], Xiaojing Liu [b], Tong Sun [c], Kenneth T.V. Grattan [c], Jie Zhao [a]

[a] State Key Laboratory of Robotics and Systems, Harbin Institute of Technology, Harbin, PR China
[b] Department of Oral and Maxillofacial Surgery, Peking University School and Hospital of Stomatology, National Engineering Laboratory for Digital and Materials Technology of Stomatology, Beijing Key Laboratory of Digital Stomatology, Beijing 100034, PR China
[c] School of Engineering & Technology, City, University of London, Northampton Square, London, ECIV OHB, United Kingdom

Abstract: Shape sensing is of importance for the manipulation of flexible needles. In this work, a 0.6 mm diameter stylet with five Fiber Bragg Gratings (FBGs) installed as triplets was designed and implemented and a novel model of local curvature was established. A gradient-based optimization method has been integrated into the complete algorithm for shape sensing and this was used to reduce the difference between the midpoint curvature and the mean curvature. The experimental results obtained show that the mean tip errors are 0.35mm, 0.30mm, 0.38mm in the single-bending, double-bending and space-bending experiments, respectively. In a torsion test experiment which was performed, when the rotation angle of the tip was less than 25°, the error seen was less than 0.5mm. Furthermore, when the needle designed in this work was used to puncture a 60mm thickness, *ex vivo* biological tissue, the mean error of the measurement of the needle tip was 0.39mm.

Keywords: Fiber Bragg Gratings (FBGs), shape sensing, flexible needle, local curvature, gradient-based optimization

1 Introduction

The accurate placement of needles is a critical process during different types of surgeries, such as biopsies, brachytherapy, and radiofrequency ablation. Such accurate placement of the needle is easily made possible if any deformation of the needle used can be neglected. However, in 'real world' situations, some deformation of the needle is inevitable during surgeries and a knowledge of the deformation that occurs is even sometimes utilized to target lesions that cannot be reached along a straight path. To do so in a reproducible way, steerable flexible needles have been proposed. The flexibility of the needles used during these surgeries depends on both the shape of the needle and the position of the tip – and this should be known (and therefore measured accurately) in real time. Several medical image-based methods, such as using Ultrasound (US), Computed Tomography (CT) and Magnetic Resonance Imaging (MRI), for example, have been employed to measure the shape of such needles when inserted into tissue. By comparison with using both CT and MRI methods, using Ultrasound can provide the advantage of real-time feedback of the position of the needle tip, especially allowing the surgeon to prevent the needle from damaging vital nerves or blood vessels. It can be noted that it is difficult to obtain sufficient accuracy in the position of the needle *in situ*, when using the Ultrasound method. A considerable number of studies have been reported in recent decades which have attempted to improve both the accuracy and the usability of this method. An alternative is the electromagnetic tracking method which can offer high-resolution, real-time feedback on the position of the needle tip, and give data on it in a more intuitive manner.

However, this method has not been widely used in clinical practice up to now, due to problems of electromagnetic compatibility. Both these methods (using ultrasound and electromagnetic tracking) ignore the measurement of the actual shape of the full length of the needle, as they focus mainly on real-time feedback which defines the position of only the needle tip – a problem as the shape of the full length of the needle is needed and this is not given by the real-time feedback received in these methods. In this work, a method for shape sensing using Fiber Bragg Gratings (FBGs) integrated along the full length of a needle has been proposed, as this method shows promise to meet accuracy requirements required for *in vivo* tracking of surgical instruments, taking advantage of the excellent properties of the FBGs used, such as immunity to external electromagnetic fields, small dimensions, low mass, robustness and their multiplexing capabilities[1–4].

Several studies have previously been carried out using FBGs to track the position of surgical instruments, including needles, although the application scenarios and configurations of FBGs used and reported in the literature are different from those in this study. Previous methods have been based on the linear relationship seen between the Bragg wavelength of the FBGs used and the strain resulting from the deformation of the instrument. The local curvature has then been estimated by making a reasonable assessment of the situation, based on the number and position of the FBGs used in the instrument, as for example has been reported by Gander *et al.* [5]. Park *et al.* first proposed the use of FBGs for shape sensing of needles [6], where this work provided a basis for detailed shape sensing, involving the configurations of the FBGs, the filtering of the signals received, the creation of a model of the local curvature, the calibration of the model, the interpolation of the positions on the curvature and thus the description of the overall shape. The FBGs were usually configured as triplets in many of the reported studies [6–12], where such triplets were fixed on the surface of the needles or the other instruments used. Such a configuration is the simplest theoretically, which can be used in estimating the magnitude of the curvature and the direction of the bending, while excluding the effects of other disturbances such as temperature-induced Bragg wavelength shifts. Some recent studies have added a further FBGs (placed in the centre of the triplets) [13–19], to provide more detailed information to include in the model, especially information on the torsional strain [14, 18] and axial tension [15, 20]. The FBGs in the centre allow independent compensation for temperature and axial strain, allowing the torsion alone to be calculated – this being extremely useful in those applications where knowing the tip position and pose is critical despite its high cost. Further, filtering of the signal received is necessary, especially for the dynamic feedback on any changes that occur to the shape of the needle. Donder *et al.* [21] and Lu *et al.* [20] have implemented shape sensing of steerable needles and catheters, respectively, using Extended Kalman Filtering (EKF). These studies have shown that EKF offers a better dynamic response than using other filters, such as the median filter and the mean filter, gradually making it a common method for shape sensing. Then it is important in the model to know local curvatures and their calibration, obtained by extracting signals of interest from the FBGs arrays used. FBGs are not only sensitive to strain, but also to temperature and humidity [22] and further Bragg wavelength shifts due to the strain caused by different types of deformation, such as bending, torsion and tension/compression are superimposed on these. All this points to the need for the establishment and accurate calibration of a model as the core of good shape sensing, and accurate data [23]. Park et al. directly constructed the relationship between the signals from the FBG arrays used and the local curvature, using a calibration matrix [6], which separated the shifts of the Bragg wavelengths caused by both the bending and the temperature, a method used in many studies [24, 25]. Moore *et al.* used a geometry-based model [8], which has the clearer physical meaning [20, 23, 26–28] and thus is more commonly used. Yi *et al.* established the angle at which the FBG arrays were packaged, as a function of the torsion-induced strain at different torsion angles [12]. Floris *et al.* have proposed a simple method, based on Saint-Venant's torsion theory for homogeneous circular cylinders, to calculate the fiber torsion [14]. However, these models usually ignore certain of the key contributing factors to the shifts of the Bragg wavelength that are measured. The model that can

simultaneously exclude temperature, axial strain and torsional strain have not yet been sufficiently studied. Finally, an interpolation of the local curvature must be made to achieve better shape sensing. When the shape is relatively simple, the use of a linear interpolation will be sufficient to ensure that the shape sensing offers good performance [16, 25] but to make the curvature smoother, the cubic spline interpolation has also been used in many studies [8, 12, 29]. In most studies, the interpolation is based on assuming that the shift of the Bragg wavelength is linear with respect to the average strain and therefore errors may be introduced when the mean curvature is calculated by assuming the average strain at the midpoint curvature of the grating [30]. Any error produced using this assumption will be noticeable when the curvature changes drastically and to our knowledge, no reports on shape sensing have taken this potential error into account. The last issue considered is how to describe the shape of the needle – whether it is a catheter or a flexible needle, only the shape of its central curvature is usually described and polynomial fitting has first been used to illustrate the shape of this curvature [6, 9, 25]. However, when many FBGs arrays are used, the boundary value is prone to the Runge phenomenon and Seifabadi *et al.* have proposed using the differential equation for elastic beam deformation to calculate the small deformation in the plane of the needle, thus effectively avoiding this phenomenon [31]. Some studies have used a series of transformation matrices to calculate the positions of the discrete points on the curve to describe large deformation curves in three-dimensional space, based on the assumption of constant local curvature [19, 29]. In recent years, using a moving frame approach based on differential geometry has attracted interest, mainly including the Frenet-Serret frame [7, 8, 10] and the Bishop frame [16, 18, 32, 33]. Although it has been shown that those methods based on the homogeneous transformation matrix are less sensitive to the accuracy of interpolation than are the methods based on a moving frame [19], it is clear that the moving frame methods are more suitable for generalization to other shape-based studies, than, for example, force sensing from the shape of deformed objects [34].

In this work, a new approach has been taken in which FBGs were embedded on a flexible needle, in the form of triplets, and a complete solution for shape sensing is proposed. The contributions that this work makes can be summarized as follows: 1) A novel model for the local curvature has been proposed that can separate the shifts of the Bragg wavelength caused by bending from those due to other factors, including temperature, tension/compression and torsion. An appropriate calibration method and several devices, adapted to the model, have been developed to improve the accuracy of shape sensing as a result. 2) A gradient-based algorithm has been applied to the optimization of the interpolation, to redress the inconsistency highlighted above in the assumption of the mean curvature being at the midpoint of the FBGs triplets used.

The article is organized as follows. Section 2 firstly introduces the configuration of the flexible needle embedded with the FBGs triplets. The model of local curvature is then proposed, based on analysing the deformation of the needle. Section 3 proposes an optimization-based shape sensing algorithm, which introduces a gradient-based optimization method in the interpolation of curvature. Section 4 elaborates the experimental setups and results, and which is then divided into four parts, as discussed below. This begins with the calibration experiment carried out, followed by the results obtained. Then, based on the results of this calibration, the needles designed by the authors were individually subjected to a test involving only bending, only torsion and then an *in vitro* biological tissue puncture test. Section 5 completes the paper, with conclusions drawn on the work.

2 Design and modelling of the flexible needles

2.1 Design of the needle with the embedded FBGs

The needle designed in this work consisted of a stylet and a cannula, as shown in Fig. 1(a), which are similar in construction to the puncture needles used in a typical clinical environment. Both the stylet and the cannula are made of Nitinol (provided by PEIERTECH Co., Ltd). The inner diameter of the cannula used was 0.8mm and the outer diameter was 1mm. The stylet was 0.6mm in diameter and three

grooves (width, 0.2mm and depth, 0.2mm, as detailed in Fig. 1(b)) were cut (using electrical discharge machining (EDM)) to accommodate the fibers, as shown in Fig. 1(a). The grooves were all manufactured at one time, clamping the set up using the same length of electrode as the grooves. Three 0.15mm diameter fibers were fixed in the groove, respectively, using epoxy adhesive (type, Loctite 1C-LV). Each fibre was inscribed with five FBGs (of 10 mm length with an interval of 35 mm between each), using a phase mask technique (as provided by Beijing Tongwei Technology Co., Ltd). The Bragg wavelengths of these five FBGs used were 1530nm, 1540nm, 1550nm, 1560nm and 1570nm respectively. The FBGs in the same position on the three fibres were aligned and are referred to as a triplet. The stylet and the cannula both have plastic housings fixed to the root and are used in the form of trocars. Such a structure not only avoids direct contact between human tissue and the adhesive, but also reduces the frictional resistance as its sharp tip can cut through the tissue to reduce the axial force. This means that only a small fraction of the strain due to the tension/compression and torsion are transferred to the stylet, a condition which is essential for use in the model described below.

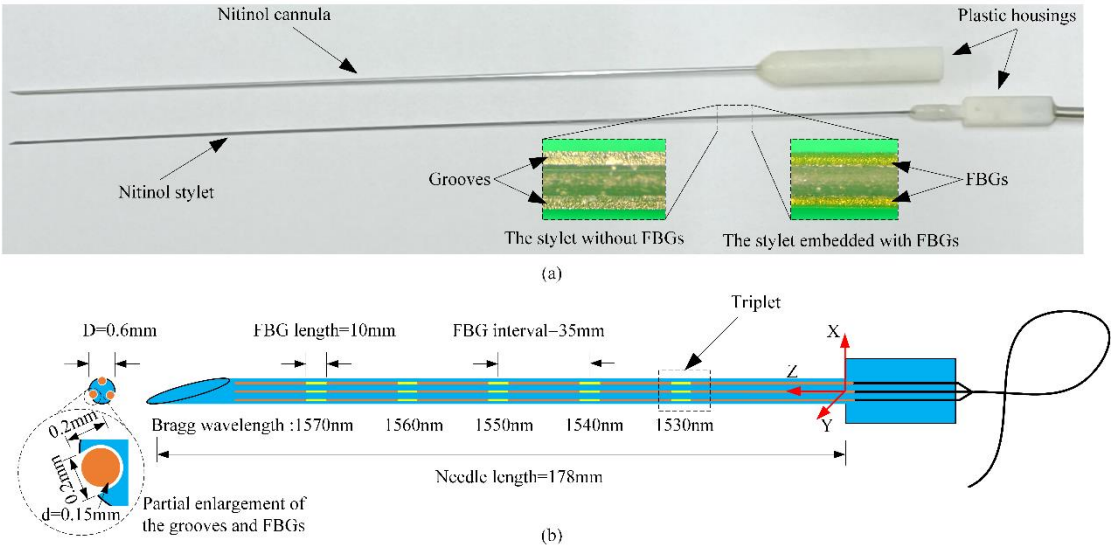

Fig. 1 Configuration of the needle with the FBGs incorporated
(a) Photograph of the cannula and stylet of the needle (with inset showing the stylet with and without the embedded FBGs) and (b) schematic of FBG triplets used in a needle of length 178mm

2.2 Model of the local curvature

It is well known that the shifts of the Bragg wavelength are mainly due to the strains of the FBGs along the axis of the fiber, and the change of the environment (mainly temperature), before any deformation (tension/compression, torsion and bending) of the needle is taken into consideration. All the wavelength shifts associated with these effects will be cumulative and result in observing a single wavelength shift. Consequently, in order to understand only the shape changes that occur, separating these shifts is important and this can be done through matching in the model created. In this section, all the major factors that cause the shifts of Bragg wavelength that were observed were classified as homogeneous or inhomogeneous, according to the perturbation analysis of the structural parameters carried out. Of these, only the Bragg wavelength shifts due to bending of the needle are inhomogeneous and based on this conclusion, a model for the local curvature of the needle has been proposed, which is insensitive to the homogeneous shifts of the Bragg wavelength. A detailed perturbation analysis has been carried out for the various causes of wavelength shift, as shown below:

1) Temperature

When monitoring the Bragg wavelength variation caused by temperature change, usually the strain caused by the thermal expansion is ignored and the expression can be simplified to:

$$\Delta\lambda_{Ti}=\Delta T\lambda_{Bi}\xi \quad (i=1,2,3) \tag{1}$$

where ξ is the refractive index of silica, and ΔT is the change of temperature, (where the subscript i is the 'serial number' of each FBG sensor in any one triplet).

Generally, the ambient temperature around a triplet will not show a large temperature gradient due to the small size of the triplet. A further consideration is that the Bragg wavelengths of the three FBG sensors of the triplet have been written deliberately so as not to be the same. The relative error caused by the perturbation, $\delta\lambda_B$, can be given as follows:

$$\frac{\delta\lambda_{Ti}}{\Delta\lambda_T}=\frac{\Delta T\xi\cdot\delta\lambda_B}{\Delta T\lambda_B\xi}=\frac{\delta\lambda_B}{\lambda_{Bi}}<10^{-3}\quad(i=1,2,3) \tag{2}$$

It is relatively easy in practice to control this perturbation to within 1 nm and therefore the relative error is less than 10^{-3}, which means that the shifts of any one triplet are homogeneous.

2) Tension/compression

To more clearly represent the relationship between the deformation of the needle and the strains measured on the FBGs, a section of length, L, in a fiber of length, l, is isolated for analysis, as shown in Fig. 2(b), in the form of a side-expansion diagram. Since the needle assembly is such that it does not guarantee that the axes of the FBG sensors and of the stylet are perfectly parallel, the introduction of the helix angle, η_i, is necessary. The relationship between the strains on the FBGs in a triplet and the shifts of the Bragg wavelength can be described as follows:

$$\Delta\lambda_i=\lambda_{Bi}(1-P_e)\varepsilon_{ai}\quad(i=1,2,3) \tag{3}$$

$$\varepsilon_{ai}=\frac{l'}{l}-1=\varepsilon_a\frac{\sin\eta_i}{\sin(\eta_i+\omega_i)}+\frac{\sin\eta_i}{\sin(\eta_i+\omega_i)}-1\quad(i=1,2,3) \tag{4}$$

where, $\Delta\lambda_i$ is the shift of the Bragg wavelength, P_e is the photoelastic coefficient, ε_{ai} is the strain on the FBG sensors, and η_i is the helical angle. Further, ω is the angle due to the tension/compression experienced and $\varepsilon_a=L'/L-1$ is the axial strain. L' and l' are defined, respectively, as the length of the section and the fiber after the deformation.

The relative error caused by the disturbance, $\delta\lambda_B$, is given as follows:

$$\frac{\delta\lambda_i}{\Delta\lambda_i}=\frac{\delta\lambda_B\cdot(1-P_e)\varepsilon_{ai}}{\lambda_B(1-P_e)\varepsilon_{ai}}=\frac{\delta\lambda_B}{\lambda_{Bi}}<10^{-3}\quad(i=1,2,3) \tag{5}$$

Further, the strain caused by the perturbation of $\delta\eta$ is given as follows:

$$\delta\varepsilon_{axial}=\left.\frac{d\varepsilon_{axial}}{d\eta}\right|_{\eta=\frac{\pi}{2}}\cdot\delta\eta=0 \tag{6}$$

As can be seen, the shifts of one triplet caused by tension/compression are also homogeneous.

3) Torsion

The strain due to the torsion experienced is as shown in Fig. 2(a) and Fig. 2(c) in the form of a side expansion diagram, as expressed as Eq. (7) and Eq. (8), as shown below.

$$\varepsilon_{ti}=\sqrt{1+(\sin\eta_i)^2\left(\tan\gamma_i\right)^2+\sin(2\eta_i)\tan\gamma_i}-1\quad(i=1,2,3) \tag{7}$$

$$\tan\gamma_i=r_i\theta \tag{8}$$

where, ε_{ti} are the strains of the three FBGs (i = 1,2, 3) due to torsion, and γ_i is the angle experienced due to torsion. θ is the torsion angle per unit length and r_i is the distance from the center of each fiber to the center of the stylet.

The torsion angle usually is relatively small. Although some studies have claimed that the rotation of the needle in the tissue can cause non-negligible torsion of the needle, the structure of the trocar makes it difficult to transmit the torsion, if any, to the stylet. The high-order small quantities in the Taylor expansion of Eq. (7) at $\theta=0$ have been omitted. As a result, the strain can be approximated as shown below

$$\varepsilon_{ti} = \frac{1}{2}\sin(2\eta_i) r_i \theta + \frac{1}{2}(\sin^2\eta_i r_i^2 - \frac{1}{4}\sin^2(2\eta_i) r_i^2)\theta^2 \quad (i=1,2,3) \tag{9}$$

The relative errors caused by the perturbation, $\delta\eta$, are as follows:

$$\frac{\delta\varepsilon_{ti}}{\varepsilon_{ti}} = \frac{\left.\frac{d\varepsilon_{ti}}{d\eta}\right|_{\eta=\frac{\pi}{2}} \cdot \delta\eta}{\varepsilon_{ti}} = \frac{-\delta\eta}{\frac{1}{2}\sin(2\eta_i) + \frac{1}{2}(\sin^2\eta_i r_i - \frac{1}{4}\sin^2(2\eta_i) r_i)\theta} \quad (i=1,2,3) \tag{10}$$

Thus for one single FBG sensor, it can be seen from Eq.10 that η_i has a significant effect on the strain, due to torsion, especially when r_i and θ are small. This means that when the helix angle becomes smaller, the FBG is more sensitive to torsion. Furthermore, for the needle designed in this work, since r_i is small, the requirements for $\delta\eta$ is more demanding. Thus, the perturbation, $\delta\eta$, may cause the strain on the three FBG sensors in the triplet to be inhomogeneous.

The relative error caused by the perturbation, δr, is as follows:

$$\left.\frac{\delta\varepsilon_{ti}}{\varepsilon_{ti}}\right|_{\eta_i=\frac{\pi}{2}} = \frac{\left.\frac{d\varepsilon_{ti}}{dr}\right|_{r=r_i} \cdot \delta r}{\varepsilon_{ti}} = \frac{2\delta r}{r_i} \quad (i=1,2,3) \tag{11}$$

Based on the structure of the needle, δr has a maximum value of 0.05mm and the design size used for r_i is 0.2mm – that is to say, the perturbation of r_i may cause the strain on the three FBG sensors in the triplet to be inhomogeneous. In other words, a calibration of r_i is essential for these applications, requiring *precise measurement* of torsion, especially when the r_i is small.

However, this work does not focus on calculating the exact value of the torsion. For the needle that was designed in this work, the maximum value of $\frac{\pi}{2}-\eta_i$ is $(0.2-0.15)/10 = 5\times10^{-3}$ which is guaranteed by the machining process used. According to Eq. (9) it can be seen that $\varepsilon_{ti} \approx 1\times10^{-6}\theta + 2\times10^{-8}\theta^2$. Since the strain is very small when θ is small, it is difficult for the interrogator to discern this inhomogeneity. Thus, while the strain due to the torsion is inhomogeneous, it can still be modelled as homogeneous when θ is small. However, there is a potential risk that this assumption will not hold, as θ increases.

4) Bending

A schematic of both the bending and related structural parameters are presented in Fig. 2(a) and Fig. 2(d). The x-z plane is regarded as the reference plane, that is, the virtual neutral plane when there is no bending. The strain due to pure bending can be written as:

$$\begin{bmatrix} \varepsilon_{b1} \\ \varepsilon_{b2} \\ \varepsilon_{b3} \end{bmatrix} = \begin{bmatrix} \sin\alpha_1 r_1 & -\cos\alpha_1 r_1 \\ \sin\alpha_2 r_2 & -\cos\alpha_2 r_2 \\ \sin\alpha_3 r_3 & -\cos\alpha_3 r_3 \end{bmatrix} \begin{bmatrix} -\cos\beta\cdot\kappa \\ -\sin\beta\cdot\kappa \end{bmatrix} \tag{12}$$

where ε_{b1} ε_{b2} and ε_{b3} are the strains caused by bending, α_1, α_2 and α_3 are the angles of r_1, r_2 and r_3 with respect to the reference plane. β is the angle of the neutral plane with respect to the reference plane, and κ is the local curvature. Additionally, $\cos\beta\cdot\kappa$ and $\sin\beta\cdot\kappa$ also are termed the projected curvatures i.e., the projections of the curvature on the reference plane.

The relative errors caused by the perturbation, $\delta\alpha$, are as follows:

$$\left.\frac{\delta\varepsilon_{bi}}{\varepsilon_{bi}}\right| = \frac{\left.\frac{d\,\delta\varepsilon_{bi}}{d\alpha}\right|_{\alpha=\alpha_i}\cdot\delta\alpha}{\varepsilon_{bi}} = \frac{\delta\alpha}{\tan(\alpha_i-\beta)} \quad (i=1,2,3) \tag{13}$$

The values of α of the three FBG sensors in any one triplet must be different, which is also the reason for the inhomogeneity that occurs. From another perspective, the result of this analysis shows that the sensitivity of this method for shape sensing, to the orientation of the device, is nonlinear.

The relative errors caused by the perturbation, δr, are as follows:

$$\frac{\delta\varepsilon_{bi}}{\varepsilon_{bi}} = \frac{\left.\frac{d\,\delta\varepsilon_{bi}}{dr}\right|_{r=r_i}\cdot\delta r}{\varepsilon_{bi}} = \frac{\delta r}{r_i} \quad (i=1,2,3) \tag{14}$$

Obviously, the values of r_i in one triplet cannot be considered to be the same, in terms of the stylet.

The strains of the triplet due to bending shows a different pattern from what is seen in the previous ones, which are inhomogeneous. That means the structural parameters, α_i and r_i, must be calibrated.

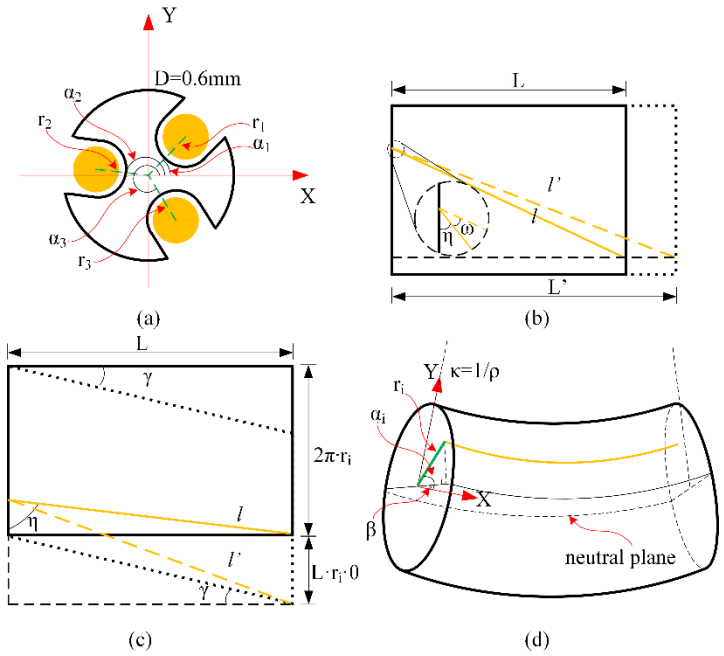

Fig. 2 A segment of the stylet with the FBGs triplets used

(a) Structural parameters of the cross section. r_1, r_2 and r_3 is the distance from the center of each fiber to the center of the stylet. α_1, α_2 and α_3 is the angle of r_1, r_2 and r_3 relative to the referenced plane (x-z plane).

(b) The geometric relationship of the stylet after tension/compression is represented by the expansion diagram. L and L' are the length of the section before and after the deformation respectively. l and l' is the length of the fiber. η is the helical angle. ω is the angle due to tension/compression.

(c) Geometric relationship about the torsion of the stylet. γ is the angle due to torsion. θ is the torsion angle per unit length.

(d) Geometric relationship about the bending of the stylet. κ is local curvature. ρ is the radius of local curvature.

To summarize, it is only the bending which allows the shifts of the wavelength of the Bragg gratings in a triplet to be inhomogeneous, when the torsion angle is small. As a result, a complete model of the local curvatures has been proposed, as can be seen in Eq. (15). Here it is clear that the shifts of the Bragg wavelength caused by the bending can be distinguished from those caused by the temperature, the tension/compression and the torsion,

$$\begin{bmatrix} \Delta\lambda_1 \\ \Delta\lambda_2 \\ \Delta\lambda_3 \end{bmatrix} = \begin{bmatrix} \zeta_B \sin\alpha_1 r_1 & -\zeta_B \cos\alpha_1 r_1 & 1 \\ \zeta_B \sin\alpha_2 r_2 & -\zeta_B \cos\alpha_2 r_2 & 1 \\ \zeta_B \sin\alpha_3 r_3 & -\zeta_B \cos\alpha_3 r_3 & 1 \end{bmatrix} \begin{bmatrix} -\cos\beta \cdot \kappa \\ -\sin\beta \cdot \kappa \\ \Delta\lambda_T + \zeta_B(\varepsilon_t + \varepsilon_{axial}) \end{bmatrix} \tag{15}$$

where $\zeta_B = \lambda_B(1 - P_e)$. The first part of the equation, on the right side of Eq. (15), represents the structural parameters of the triplet, which can be calibrated using the method which will be described in Section 4.1. This model shows that it is possible to exclude the homogeneous parts, without affecting the central FBGs.

3 Algorithm of shape sensing

In this section, an algorithm for shape sensing using the model of the local curvature has been proposed, which includes the filtering of the local curvatures, the optimization according to the results of the interpolation and the description of the shape, based on the Bishop Frame, as shown in Fig. 3. First, the shifts of the Bragg wavelengths of each triplet were used to calculate the values of β, κ and $\Delta\lambda_H$ with the noise in the signal present, and using the model discussed in Section 2. It can be noted that the Extended Kalman Filter (EKF) has been used for improving the accuracy of the measurement of the local curvatures. Following that, all the local curvatures were interpolated, to obtain each of the discrete curvatures, with sufficient resolution. Here, the shifts of the Bragg wavelength in the first step can only reflect the average curvatures. However, when the interpolated curve representing the curvatures is convex, the value of the average curvature can be taken as the midpoint curvature of the triplets, and this could introduce errors. Therefore, a gradient-based optimization process has been introduced to adjust the interpolation curve, so that the mean curvature seen from the interpolated curve of the curvature, over the range of the triplets, matches the curvature measured. Finally, the shape of the needle can be described, based on the Bishop Frame. An important reason to choose the Bishop Frame is to eliminate the singularities which appear in the Frenet Frame [32]. The following sections give a detailed description of the three steps taken.

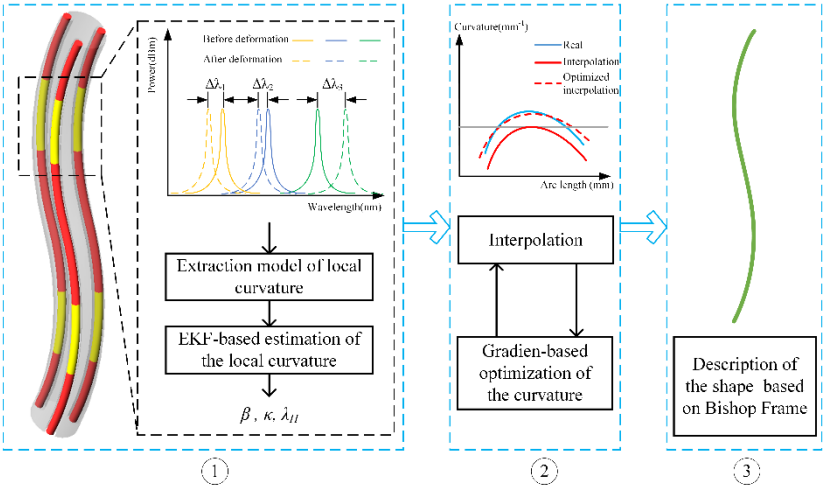

Fig. 3 Flow of the shape sensing procedure

The first step was to filter the local curvature for a single triplet. The second step was to interpolate and optimize the discrete curvatures. Taking a triplet as an example, when the curvature interpolation curve is convex, if the real curvature is as shown by the blue line, then the interpolation curve is as shown by the gray line, when the average curvature is taken as the midpoint curvature of the triplet. The goal of the optimization is thus to adjust the gray line to be as close as possible to the red line, where the mean curvature of the interpolated curve is closer to the measured value. The central line of the needle is described, based on the Bishop Frame.

3.1 Filtering of the local curvature

In order to describe this more easily, some symbols that were used in Eq. (15) are replaced, as shown below in Eq. (16)

$$\begin{bmatrix} \Delta\lambda_1 \\ \Delta\lambda_2 \\ \Delta\lambda_3 \end{bmatrix} = \begin{bmatrix} C_{11} & C_{12} & 1 \\ C_{21} & C_{22} & 1 \\ C_{31} & C_{32} & 1 \end{bmatrix} \begin{bmatrix} -\cos\beta\cdot\kappa \\ -\sin\beta\cdot\kappa \\ \Delta\lambda_H \end{bmatrix} \tag{16}$$

where, $\Delta\lambda_H$ is the homogenous shifts of the Bragg wavelengths for a triplet of FBGs. The state vector at an instant, k, for each FBG triplet can be defined as shown:

$$\mathbf{x}_k = \begin{bmatrix} \kappa_k & \beta_k & \Delta\lambda_{H,k} \end{bmatrix}^{\cdot} \tag{17}$$

The state transition model can be formulated as:

$$\mathbf{x}_{k+1} = \mathbf{A}\mathbf{x}_k + \mathbf{w}_k \tag{18}$$

where $\mathbf{A}=\mathbf{I}_{3\times3} \in \mathrm{R}^{3\times3}$ for this quasi-static measurement, $\mathbf{w}_k \sim (0,\mathbf{Q}) \in \mathrm{R}^3$ is the process noise with covariance $\mathbf{Q} \in \mathrm{R}^{3\times3}$. A reference initial value is $\mathbf{Q} = \mathrm{diag}(0.1,100,0.1)$. The shifts are therefore measured to be:

$$\mathbf{z}_k = \begin{bmatrix} \Delta\lambda_1 & \Delta\lambda_2 & \Delta\lambda_3 \end{bmatrix}^{\cdot} \tag{19}$$

The observation model can be formulated as:

$$\mathbf{z}_k = h(\mathbf{x}_k) + \mathbf{v}_k \tag{20}$$

where $\mathbf{v}_k \sim (0,\mathbf{R}) \in \mathrm{R}^3$ is the observation noise with covariance $\mathbf{R} \in \mathrm{R}^{3\times3}$, and a reference initial value is given by $\mathbf{R} = \mathrm{diag}(1,1,1)$, $h(\mathbf{x}_k)$ is extended from Eq. (16). The prior estimate of the state vector and the covariance is given by:

$$\hat{\mathbf{x}}_{k|k-1} = \mathbf{A}\hat{\mathbf{x}}_{k-1|k-1} \tag{21}$$

$$\mathbf{P}_{k|k-1} = \mathbf{A}\mathbf{P}_{k-1|k-1}\mathbf{A}^{\cdot} = \mathbf{Q} \tag{22}$$

The Kalman gain, $\mathbf{K}_k$, can be calculated as:

$$\mathbf{K}_k = \mathbf{P}_{k|k-1}\mathbf{H}_k^{\cdot}\left(\mathbf{H}_k\mathbf{P}_{k|k-1}\mathbf{H}_k^{\cdot} + \mathbf{R}\right)^{-1} \tag{23}$$

where $\mathbf{H}_k$ is linearized from $h(\hat{\mathbf{x}}_{k|k-1})$ as shown below:

$$\mathbf{H}_k = \left.\frac{\partial h}{\partial \mathbf{x}}\right|_{\hat{\mathbf{x}}_{k|k-1}}$$

$$= \begin{bmatrix} -C_{11}\cos\hat{\beta}_{k|k-1} - C_{12}\sin\hat{\beta}_{k|k-1} & C_{11}\sin\hat{\beta}_{k|k-1}\cdot\hat{\kappa}_{k|k-1} - C_{12}\cos\hat{\beta}_{k|k-1}\cdot\hat{\kappa}_{k|k-1} & 1 \\ -C_{21}\cos\hat{\beta}_{k|k-1} - C_{22}\sin\hat{\beta}_{k|k-1} & C_{21}\sin\hat{\beta}_{k|k-1}\cdot\hat{\kappa}_{k|k-1} - C_{22}\cos\hat{\beta}_{k|k-1}\cdot\hat{\kappa}_{k|k-1} & 1 \\ -C_{31}\cos\hat{\beta}_{k|k-1} - C_{32}\sin\hat{\beta}_{k|k-1} & C_{31}\sin\hat{\beta}_{k|k-1}\cdot\hat{\kappa}_{k|k-1} - C_{32}\cos\hat{\beta}_{k|k-1}\cdot\hat{\kappa}_{k|k-1} & 1 \end{bmatrix} \tag{24}$$

Finally, the estimation of the state vector and the updated covariance is given by:

$$\hat{\mathbf{x}}_{k|k} = \hat{\mathbf{x}}_{k|k-1} + \mathbf{K}_k\left(\mathbf{z}_k - h(\hat{\mathbf{x}}_{k|k-1})\right) \tag{25}$$

$$\mathbf{P}_{k|k} = (\mathbf{I}_{3\times3} - \mathbf{K}_k\mathbf{H}_k)\mathbf{P}_{k|k-1} \tag{26}$$

3.2 Interpolation and optimization of the curvature

Normally, the shape of the needle is considered to be smooth and continuous. However, the load at the base and at the tip of the needle is abrupt, that is, here the curvature has changed significantly and so it is extremely difficult to measure the curvature at these two positions. So, the curvatures of the two positions were considered to be zero in some research work done on shape sensing of flexible needles and admittedly this assumption is usually valid, especially at the needle tip. Nevertheless, here the load applied to the needle has been analyzed and it has been concluded that it is more appropriate to estimate the curvatures linearly, especially at the base. The classical force analysis of the situation following needle penetration into the tissue, as reported by Misra et.al. [35], is shown in Fig.4. Although the loads on the needle and the deformation of the needle are complex in the tissue, there is usually only a small lateral displacement at the piercing point. For this reason, the base of the needle to the piercing point can be viewed in a simplified way as a cantilever beam subjected to a concentrated force and a concentrated force couple. Naturally, the curvature is linear with respect to the arc length. Such a simplification can further improve the accuracy of the measurement of the tip position, than can be done simply by considering the curvature at the base to be zero, because the error at the base will be amplified as the arc length increases. In contrast, the curvature at the tip has much less effect on the tip position. Based on this conclusion, a cubic spline interpolation with natural boundary conditions was then chosen to take into account the smoothness of the curvature and the linear estimation of the boundary.

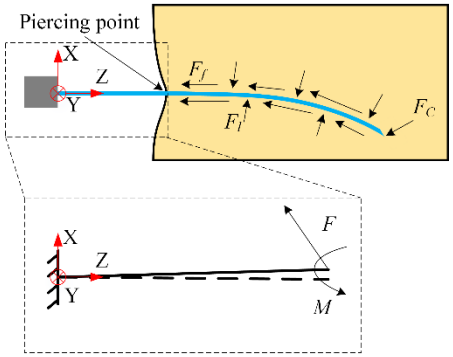

Fig. 4 Schematic diagram of the load applied to the needle

(F_f, the friction force between needle and the tissue, F_l, the lateral force due to the deformation of the needle, F_c, the cutting force during the penetration. F, the concentrated force, M, the concentrated force couple.)

Another issue that cannot be ignored in the analysis is the uneven strain on the FBG triplets along the axis [30], because the signal returned by the FBG interrogator only reflects the average strain. The curvature of the midpoint of the triplets is equal to the mean curvature, when the curvature is linear with respect to the arc length. However, this equivalence introduces errors when the curvature is convex with respect to the arc length, as shown in Fig. 5. Therefore, a method of gradient-based optimization has been proposed to improve this situation. Here $\boldsymbol{\kappa}_M = \begin{bmatrix} \kappa_{M1} & \kappa_{M2} & \cdots & \kappa_{Mn} \end{bmatrix}$ is defined as shown and represents the set of mean curvatures, measured by n FBG triplets and $\boldsymbol{\kappa}_O^{(k)} = \begin{bmatrix} \kappa_{O1}^{(k)} & \kappa_{O2}^{(k)} & \cdots & \kappa_{On}^{(k)} \end{bmatrix}$ represents the midpoint curvature of n FBG triplets, after each step of optimization carried out. The initial value of $\boldsymbol{\kappa}_O^{(0)}$ is equal to $\boldsymbol{\kappa}_M$. The average value of the interpolation function of the curvature is given by $\boldsymbol{\kappa}_A^{(k)} = \begin{bmatrix} \kappa_{A1}^{(k)} & \kappa_{A2}^{(k)} & \cdots & \kappa_{An}^{(k)} \end{bmatrix}$, calculated by the interpolation of $\boldsymbol{\kappa}_0$. $\kappa_{Ai}^{(k)}$ has been calculated using the method of discrete integration of the results of the interpolation of $\boldsymbol{\kappa}_O^{(k)}$ over the interval of the FBG triplet. Here κ_{An} represents the projection of the curvature, $-\cos\beta \cdot \kappa$ or $-\sin\beta \cdot \kappa$ shown in Eq. (16). The optimization problem can now be defined as shown:

$$\text{minimize} \quad \left\| \boldsymbol{\kappa}_A - \boldsymbol{\kappa}_M \right\| \tag{27}$$

The gradient-based iterative formulation is given below:

$$\boldsymbol{\kappa}_O^{(k+1)} = \boldsymbol{\kappa}_O^{(k)} - \delta \cdot \left(\boldsymbol{\kappa}_A^{(k)} - \boldsymbol{\kappa}_M \right) \tag{28}$$

where a reference value of δ is empirically taken to be 0.9 to achieve oscillation-free convergence.

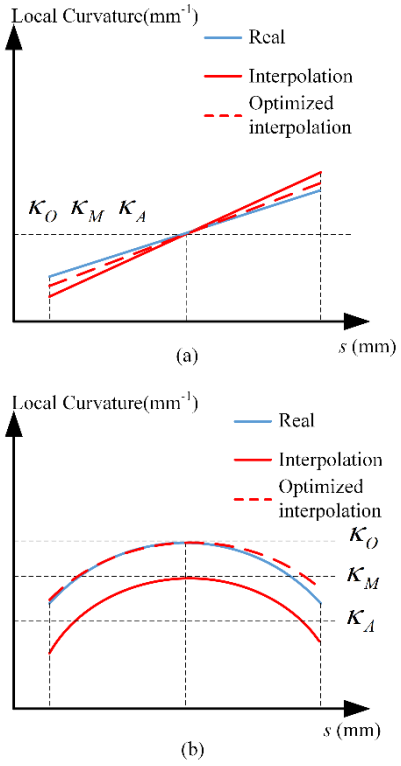

Fig. 5 Illustration of the pattern of the curvature
(a) Linear pattern (b) Convex pattern

3.3 Description of the shape of the needle

The shape of the needle can be described using the vector function of the spatial curve formed by its center, as shown

375 $$\vec{\mathbf{r}}(s) = x(s)\vec{\mathbf{i}} + y(s)\vec{\mathbf{j}} + z(s)\vec{\mathbf{k}} \tag{29}$$

376 where s is the arc length of the curve and $\vec{\mathbf{r}}(s) \in \mathrm{R}^3$.

377 In this work, the Bishop Frame, also called the parallel frame, has been applied to describe the curve.
378 Compared with Frenet Frame, it only needs quadratic differentiability and can avoid a singularity when
379 the curvature is 0. The Bishop Frame can be defined by a tangent unit vector, $\vec{\mathbf{T}}(s) = d\vec{\mathbf{r}}(s)/ds$ and two
380 normal vectors, $\vec{\mathbf{N}}_1(s)$ and $\vec{\mathbf{N}}_2(s)$. These three vectors constitute an orthogonal moving frame, and they
381 satisfy the following differential equation.

382 $$\left[\vec{T}' \quad \vec{N}_1' \quad \vec{N}_2'\right] = \left[\vec{T} \quad \vec{N}_1 \quad \vec{N}_2\right] \begin{bmatrix} 0 & -\kappa_1(s) & -\kappa_2(s) \\ \kappa_1(s) & 0 & 0 \\ \kappa_2(s) & 0 & 0 \end{bmatrix} \tag{30}$$

383 where $\kappa_1(s) = -\cos\beta(s)\cdot\kappa(s)$, $\kappa_2(s) = -\sin\beta(s)\cdot\kappa(s)$ can be obtained from the work reported in
384 Section 3.2.
385 Letting $X(s) = \left[\vec{T}(s) \quad \vec{N}_1(s) \quad \vec{N}_2(s) \quad \vec{r}(s)\right]$,

386 $$\frac{d}{d(s)} X(s) = X(s)\cdot A(s) \tag{31}$$

387 $$A(s) = \begin{bmatrix} 0 & -\kappa_1(s) & -\kappa_2(s) & 1 \\ \kappa_1(s) & 0 & 0 & 0 \\ \kappa_2(s) & 0 & 0 & 0 \\ 0 & 0 & 0 & 0 \end{bmatrix} \tag{32}$$

388 The discretized solution to Eq. (32) is given as:

389 $$\begin{cases} X(s+\Delta s) = X(s)\exp(A(s)\cdot\Delta s) \\ X(0) = \begin{bmatrix} 0 & 1 & 0 & 0 \\ 0 & 0 & 1 & 0 \\ 1 & 0 & 0 & 0 \end{bmatrix} \end{cases} \tag{33}$$

390
391 **4 Experimental work and results obtained**
392 In order to ensure the accuracy of the shape sensing carried out, experiments to calibrate the system were
393 performed first, including the parameters of the model proposed in Section 2.2 and the axial positions of
394 the FBG triplets. Following that, and based on the results of that calibration, a test of the accuracy of the
395 shape sensing was carried out. To do so, discrete lateral forces were applied to the needle, to simulate
396 three possible bending patterns of the needle when used in tissue. Besides that, torsion was applied
397 individually to the stylet, to test the limit of the rotation angle. Finally, an *ex vivo* sample of pork tissue
398 was used to simulate human tissue, to test the accuracy of the shape sensing under continuous loading in
399 this way.
400
401 **4.1 Calibration of the system**
402 The calibration procedure was divided into two steps. The first step was the calibration of the model of
403 the local curvature. To do so, a calibration device designed by the authors for this purpose was used – it
404 consists of a pair of aluminium moulds and an absolute encoder, as shown in Fig. 6. In this device, the
405 aluminium moulds were machined with a set of high-precision semi-circular grooves of constant
406 curvature, using a Computer Numerical Controlled (CNC) machine tool. The two symmetrical moulds
407 together could completely lock the stylet in the groove, to ensure that the curvature of the stylet was

exactly the same as the grooves. The setting of the absolute encoder (type, DF30, Jilin Province Sansheng Sensing Technology Co., Ltd) can be used to measure β, (as seen in Eq.(16)).

During the calibration process the stylet passed through the absolute encoder into each of the grooves in the mould. Next the stylet was manually rotated, at four random angles to cover 360°, as far as possible in each groove, as discussed in our previous work [36]. The first of these angles from the encoder, at the position when the stylet in the groove shows $\kappa = 0$, was taken as the zero point of β (i.e., $\beta = 0$). In theory, the wavelengths of the FBGs will not shift, when the stylet is in the groove with $\kappa = 0$, so the average of these wavelengths was used as the reference value for calculating $\Delta\lambda$, rather than the theoretical Bragg wavelength at which the FBGs were written [37]. $\Delta\lambda_T + \zeta_B(\varepsilon_t + \varepsilon_{axial})$ is set to 0 during the calibration. That means the temperature is constant during the calibration process and the needle is placed into the calibration mold without actually being stretched and twisted. The matrix of the structural parameters has been calculated by using the least squares method.

The calibrated results of the model are as listed in Table 1. The radial positions of the FBGs used were also calculated with $P_e = 0.22$. The values of α of the FBGs fixed in the same groove have a maximum deviation of 8.81°. However, this is inconsistent with the processing technology used and should be seen as the error in the calibration. On the other hand, this result also confirms the conclusions derived from the analysis of Eq.13 – namely that this method is less sensitive to the orientation. The calibration of r obtained is close to our design value.

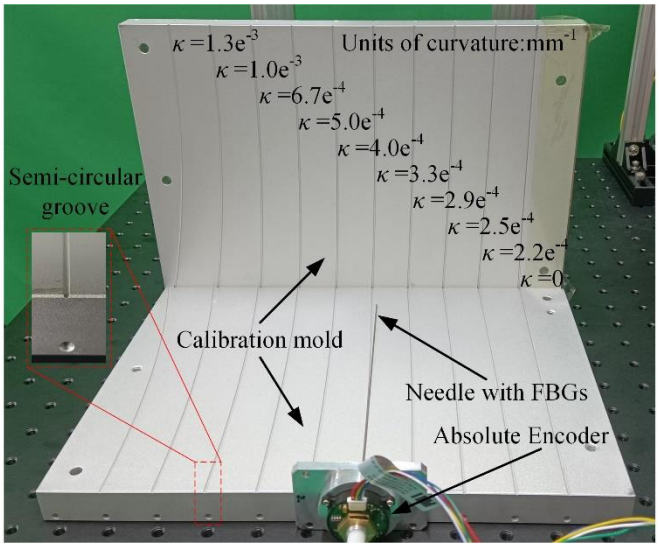

Fig. 6 Illustration of the calibration device used in this work

The second step undertaken was the calibration of the axial position of the FBG triplets, which was based on the calibration of the model of the local curvature. The etching of the gratings carried out was relatively accurate, and the error mainly comes from the process of manually fixing the FBGs to the stylet. This means that the interval between the FBG triplets does not need to be calibrated, but it is only the position of the first FBG triplet that must be calibrated. Therefore, the experimental system was designed as shown in Fig. 7. The needle designed (as discussed in Section 2) was fixed on a 2-DOF (Degrees of Freedom) platform for axial feeding (type RM-SLD-17-200-5-A) and rotation (type, RM-RT-11-360-40 provided by ROBUSTMOTION Co., Ltd). The FBGs fixed to the needle were connected to the interrogator (type TV-155, Beijing Tongwei Technology Co., Ltd.) via FC connectors. The deformation of the needle was controlled by using a loading device, which was actuated by a micrometer (type 0503-000, Qinghai Measuring & Cutting Tools Co., Ltd). The position of the needle tip was measured by a 3-axis measuring slide (type XYZLPG80, MISUMI), with an accuracy of 0.01mm. In

each measurement carried out, the probe was moved manually, until the probe tip and the needle tip were aligned.

During the calibration of the axial position of the FBG triplets, the loading device was moved near the tip of the needle and it applied an offset of about 10mm, within the assumption of a small deformation, following which the tip offset, d_m, could be measured. In addition, the tip offset could also be calculated by the method described in Section 3, and represented by d_c. The offsets in four mutually perpendicular directions were applied, and the tip offsets formed two datasets from measurements, $\mathbf{d}_m$, and calculations, $\mathbf{d}_c$. The calibration of the axial position of the first FBG triplet was described as an unconstrained optimization problem. The classical golden-section search was selected to optimize the position of the first FBG triplet in the interval, 0-20mm, to minimize Eq (34), as shown below

$$\text{minimize} \quad \left\|\mathbf{d}_m - \mathbf{d}_c\right\| \tag{34}$$

The accuracy index of the calibration in the second step was set as the interval length (and is less than 1mm). Therefore, only 7 compressions ($(0.61803)^7 \le 1/20$) are required to achieve the index value.

The search process used is shown in Fig. 8, where the error is defined as $\left\|\mathbf{d}_m - \mathbf{d}_c\right\|$. The final search interval was compressed to 14.84mm - 15.53mm, where the midpoint of the interval was chosen as the final result of the axial position listed in Table 1.

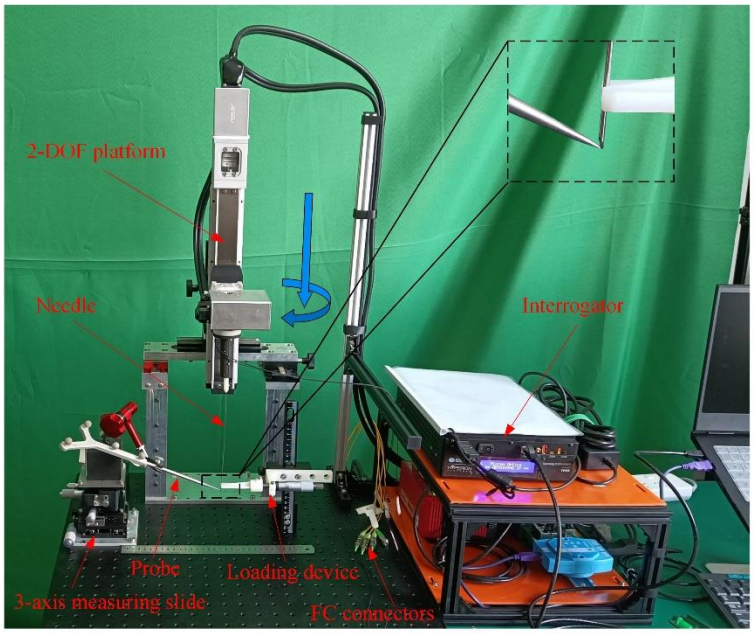

Fig. 7 Experimental system used in this work

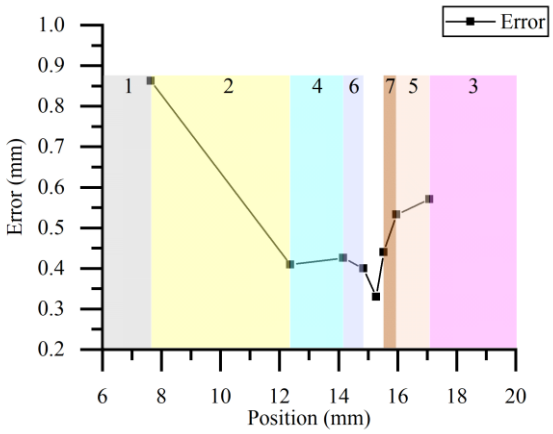

Fig. 8 Golden-section search process

(The shaded area and the numbers above it represent the interval removed during the iteration and the order of iteration, respectively. The bounds of the initial interval according to the prior determination were not calculated empirically.)

Table 1 Results of the calibration carried out

Node	Parameter matrix	α [°]	r [mm]	Position [mm]	Referential Bragg wavelength [nm]
1	$\begin{bmatrix} 204.44 & 141.07 & 1 \\ -210.37 & 82.95 & 1 \\ 25.30 & -259.19 & 1 \end{bmatrix}$	55.39 −68.48 174.43	0.208 0.189 0.218	15	1530.15 1530.18 1530.10
2	$\begin{bmatrix} 223.10 & 143.26 & 1 \\ -214.39 & 81.51 & 1 \\ 38.89 & -269.56 & 1 \end{bmatrix}$	57.29 −69.18 171.79	0.221 0.191 0.227	50	1540.12 1540.11 1540.13
3	$\begin{bmatrix} 210.91 & 138.97 & 1 \\ -237.78 & 85.89 & 1 \\ 18.03 & -295.67 & 1 \end{bmatrix}$	56.62 −70.14 176.51	0.209 0.209 0.245	85	1550.04 1550.01 1550.05
4	$\begin{bmatrix} 201.12 & 157.77 & 1 \\ -255.78 & 64.27 & 1 \\ 23.50 & -278.15 & 1 \end{bmatrix}$	51.89 −75.90 175.17	0.210 0.217 0.229	120	1560.19 1560.18 1560.12
5	$\begin{bmatrix} 154.65 & 142.53 & 1 \\ -222.156 & 93.89 & 1 \\ 44.22 & -242.40 & 1 \end{bmatrix}$	47.34 −67.09 169.66	0.172 0.197 0.201	155	1570.22 1570.33 1570.06

4.2 Bending test experiments

It is the position of the needle tip,# which is of most concern in surgeries, whether it is used to target lesions or to avoid obstacles. In addition, considering the shape sensing method discussed in this paper, the position error at each point on the curve representing the shape of the needle is magnified as the arc length increases and eventually reaches a maximum at the tip of the needle. This confirms that the position error of the needle tip was a good choice when selected as an index to evaluate the accuracy of shape sensing in this work. In order to test the accuracy of the measurements, the following experiments were designed to simulate three bending patterns in real applications under discrete loads: single bending, double bending, and spatial bending. The setup used for the experiments for the three patterns was as shown in Fig 9. The three configurations of the loading devices used could achieve three bending patterns of the needle, respectively. Furthermore, each pattern has been demonstrated from four different

directions (0° ,90° ,180° and 270°), where the directions were controlled by the rotation of the 2-DOF platform.

Only the optimized shape is shown in Fig. 9, because the difference between the optimized shape and the unoptimized shape is small. Since the main offset of the needle tip is in the x-y plane, the projection of the shape in the x-y plane was also plotted, so that the differences between the three patterns could be visualised more clearly. The errors of the tip positions obtained are as shown in Table 2. Although it is noted that a few experiments carried out show an error of >0.5mm, this appears in the double bending and spatial bending seen and overall, the mean error of each pattern is <0.5 mm, which is a satisfactory accuracy for routine CT scanning. Despite the tip errors of the optimized shape not being significantly reduced during the experiments on single bending and spatial bending, they are reduced by 0.12mm during the experiment where double bending was used. This probably occurs because the first loading point (s1=85mm) is exactly in the middle of the third triplet, as this allows the phenomenon mentioned in Section 3.2 to be more pronounced. Therefore, the gradient-based optimized interpolation proposed in this work can be used to obtain a more accurate needle tip position in shape sensing.

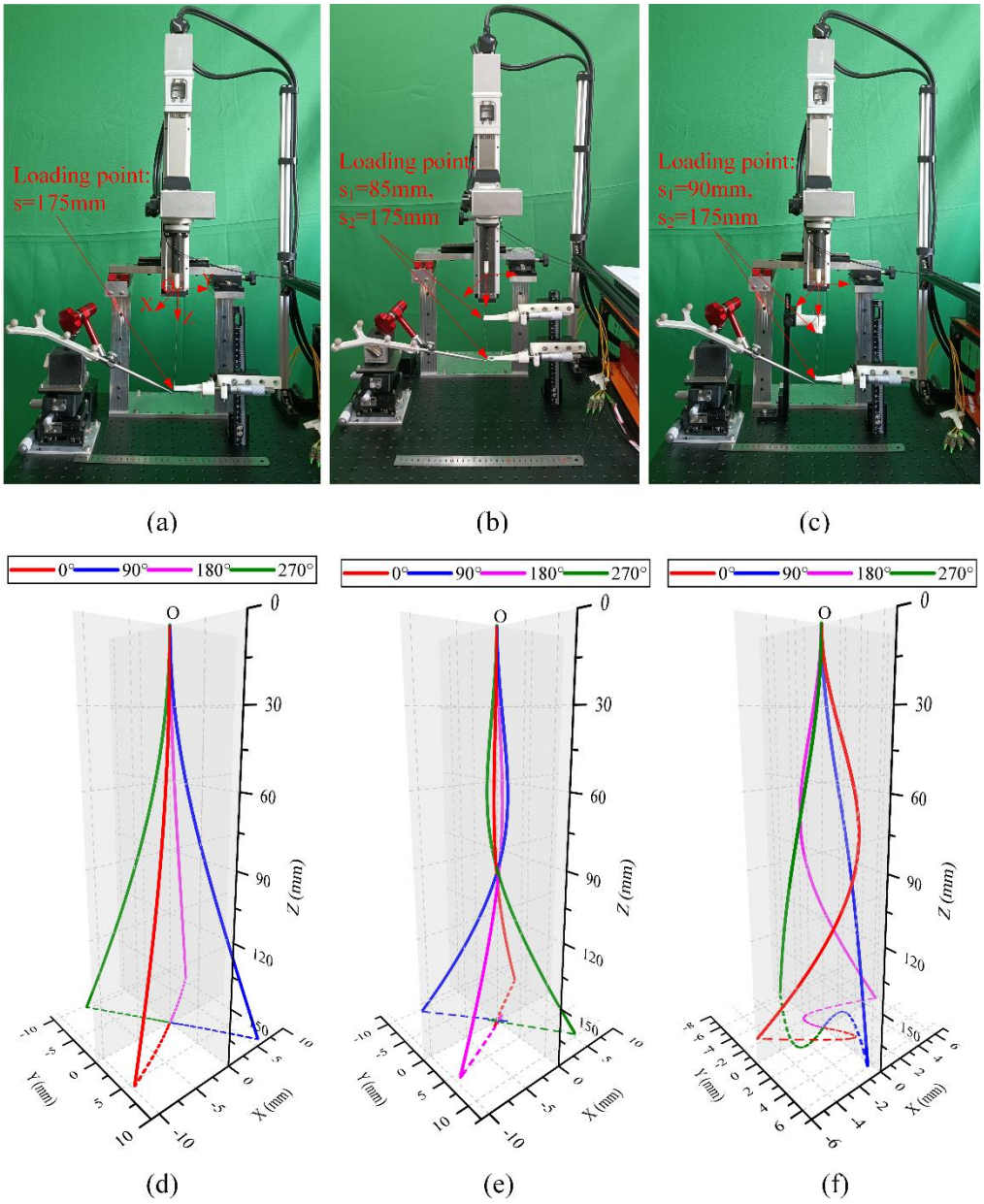

Fig. 9 Bending test

(a), (b) and (c) are photographs of the experiments using single bending, double bending and spatial bending, respectively. The positions of the loading points are expressed in arc coordinates, and only the initial value was noted because the bending does cause a change of the loading point. (d), (e) and (f) are the optimized shapes of the needle after bending, corresponding to (a), (b) and (c) respectively. Here 0°, 90°, 180°and 270° are the rotation angles of the 2-DOF platform.

Table 2 Accuracy of the Test Results
(the data in brackets represent the error of the optimized shape (used for comparison)

Direction	Tip error [mm]		
	Single bending	Double bending	Spatial bending
A	0.23(0.24)	0.29(0.18)	0.65(0.67)
B	0.26(0.27)	0.64(0.50)	0.07(0.09)
C	0.50(0.49)	0.32(0.13)	0.52(0.50)
D	0.39(0.39)	0.42(0.38)	0.22(0.25)
Mean	0.35(0.35)	0.42(0.30)	0.37(0.38)

4.2 Torsion test experiments

To verify the performance of the model for the local curvature discussed, the experimental setup shown in Fig. 10 were designed in such a way as to confirm that pure torsion, over a range of angles, does not affect the accuracy of the shape sensing reported. The stylet was isolated and then clamped by using the clamping device shown in the figure. In this way, the rotation applied by the rotary stage can simulate the possible torsion of the stylet during the process of puncturing the tissue sample and meanwhile the position of the needle tip can be considered constant. The angle of the torsion can be obtained accurately from the rotary stage, where the torsion angle was increased from 0° to 30°, in increments of 5°.

The experimental results obtained are shown in Fig. 11. It can be seen that when the rotation angle reaches 25° ($\theta = 2.45\text{rad/m}$), the tip offset increases suddenly. Before reaching 25°, the error is <0.5mm, which is still acceptable for pure torsion. Correspondingly, $\Delta\lambda_H$ for each triplet also increases as the rotation angle increases, when the rotation angle is <25°. However, this means that for a rotation angle *exceeding* 25° ($\theta > 2.45\text{rad/m}$), this will lead to the failure of the model proposed in this work. This is mainly due to the helix angle being close to 90° and the small diameter of the stylet. The reason why the initial value of $\Delta\lambda_H$ is not 0 is due on the one hand to the calibration error, and on the other the temperature difference change caused by the long time span over which the experiment was carried out.

Fig. 10 Experimental set up for the torsion test carried out

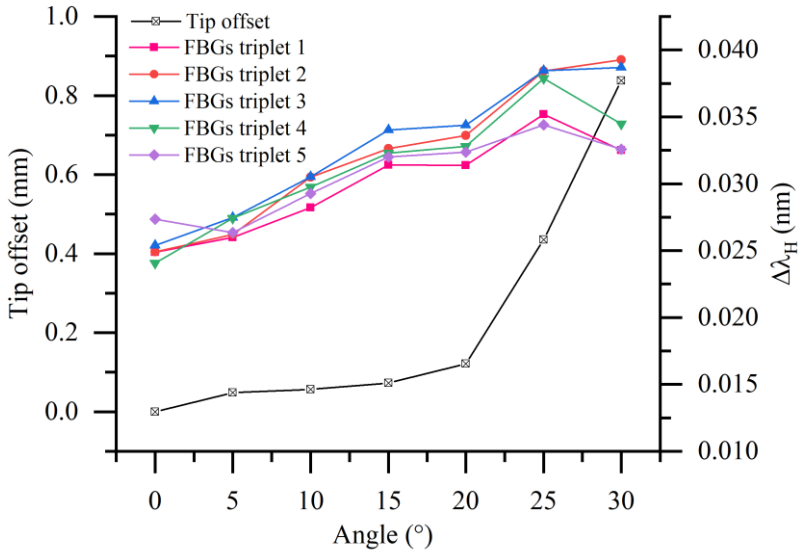

Fig. 11 Tip offset as a function of the angle (0 to 30°) caused by the torsion and $\Delta\lambda_H$ for the FBG triplets used in this work

4.4 Biological tissue puncture experiments

To more closely match the clinical applications for which the equipment would be used, a sample of *ex vivo* pork tissue was selected to further test the accuracy of the shape sensing method. The experimental setup used is shown in Fig.12(a). The 2-DOF platform was adjusted to a suitable starting position and when no tissue sample is present, the needle was driven to a specified distance where the position of needle tip at this time was measured and recorded as a reference point. Following that, the 2-DOF platform was reset, the tissue sample was placed under the needle, and the needle travelled again the specified distance. Here the thickness of the tissue was approximately 60mm and the linear feed rate was 0.3mm/s. Due to the uneven force on the single-bevel tip, the needle tip will deviate from the reference and this phenomenon is very common and unavoidable in clinical practice. These experiments were repeated four times and the results obtained from the measurements are as shown in Table 3. The maximum error of the tip offset was 0.6mm, and the average error was 0.39mm. Combining the results in Table 3 and Fig. 12(b), it can be seen that there are certain differences in the shape of the needle due to the inhomogeneity of the pork tissue used. It is clear that the effect of tissue inhomogeneity on the bending direction of the needle was reflected in two aspects of the results obtained, as follows. On the one hand, the tissue interacts with the bevel of the needle tip to generate lateral forces while on the other, the instability caused by the axial force exceeding the critical force causes the needle to deflect in any direction, where the needle is treated here as a pressure rod. This phenomenon is very likely to occur when crossing the fascia and it was also observed in the experiment. This result would seem to indicate a problem for the controllers of the steerable needles if they are purely relying on the predictions of the model.

Table 3 Results obtained from the puncture tests carried out on the tissue sample

No.	Tip offset (mm)	Error (mm)
1	14.26	0.05
2	11.67	0.6
3	14.78	0.39
4	13.24	0.53
Mean	13.49	0.39

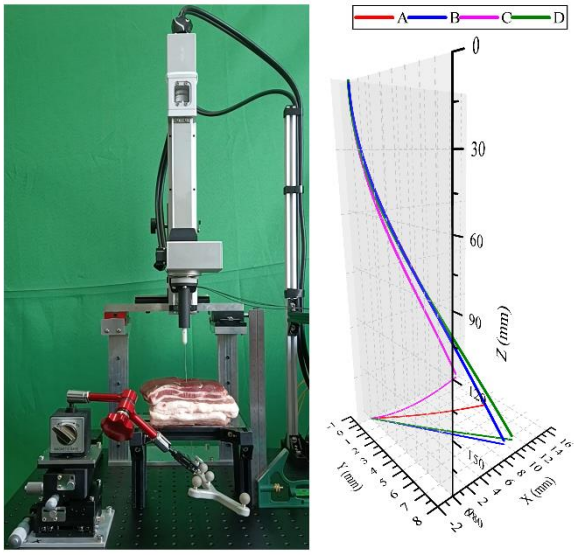

(a) (b)

Fig. 12 Experimental set up for the biological tissue puncture experiment carried out
(a) Shape sensing test using the *ex vivo* pork tissue sample.
(b) The optimized shape of the needle after puncturing the *ex vivo* pork tissue sample. Here A, B, C and D represents the results of the four experiments carried out.

5 Conclusion

In this work, a 0.6 mm diameter stylet, with five FBG triplets incorporated was designed and fabricated to measure the shape of the flexible needle. In order to improve the accuracy of the sensing of its shape, a model of the local curvature was established. In this model only the shifts of the Bragg wavelengths caused by the needle bending are inhomogeneous, which is of real importance for shape sensing in practical clinical applications. It should be pointed out that although the Bragg wavelength shift caused by torsion is considered to be homogeneous, it is limited to a certain range of torsion angle. However, it is also easy to ensure the homogeneity of these shifts by the processing technologies used, when the installation radii of the FBG sensors used are relatively large. In summary, the model for the local curvature proposed in this paper can exclude the Bragg wavelength shifts caused by temperature, tension/compression and torsion under the condition of small torsion angles, to obtain accurate measurements of the local curvature.

A further focus of this work has been to describe a complete algorithm for accurate shape sensing and to introduce gradient-based optimization in the interpolation of the curvature, based on the laws defining the deformation of the flexible needle. The experiments carried out during bending tests show that using the algorithm for shape sensing proposed, when the needle tip was offset by ~15mm under discrete loads, the errors seen are all less than 0.5mm. Gradient-based optimization reduces the mean error by 0.12mm in the experiments involving double bending: however, there is no obvious effect on the single bending and the space bending experiments carried out. The puncture experiment undertaken with *ex vivo* biological tissues have demonstrated that the method of shape sensing shows a very good performance when under continuous loading. In summary, it can be seen that the algorithm used for shape sensing proposed in this work performs better under both discrete and continuous loads. In the special case where the local curvature changes drastically, the accuracy achieved is also sufficient that it still satisfies the requirements for clinical applications, which is very satisfactory.

At present, the method discussed in this work currently only works offline. In our future work, the aim is to enable online shape sensing which would be particularly valuable in clinical applications. Given that shape prediction is particularly challenging and meaningful, future work will focus on the relationship between the force applied and the shape resulting.

Acknowledgements This research was funded by National Key Research and Development Program of China (Grant No. 2019YFB1311303 and Grant No. 2019YFB1311304), Self-Planned Task of State Key Laboratory of Robotics and System (HIT) (NO. SKLRS202207B), Grattan and Sun acknowledge support from the Royal Academy of Engineering. The authors acknowledge the support of the British Council through the 'Going Global Partnerships - Enabling Grants to Strengthen UK-China Institutional Partnerships through academic collaboration 2021' program.

References

1. Galloway KC, Chen Y, Templeton E, et al (2019) Fiber Optic Shape Sensing for Soft Robotics. Soft Robotics 6:671–684. https://doi.org/10.1089/soro.2018.0131

2. Amanzadeh M, Aminossadati SM, Kizil MS, Rakić AD (2018) Recent Developments in Fibre Optic Shape Sensing. Measurement S0263224118305608-. https://doi.org/10.1016/j.measurement.2018.06.034

3. Shi C, Luo X, Qi P, et al (2017) Shape Sensing Techniques for Continuum Robots in Minimally Invasive Surgery: A Survey. IEEE Transactions on Biomedical Engineering 64:1665–1678. https://doi.org/10.1109/TBME.2016.2622361

4. Dupont PE, Nelson BJ, Goldfarb M, et al (2021) A decade retrospective of medical robotics research from 2010 to 2020. Science Robotics. https://doi.org/10.1126/scirobotics.abi8017

5. Gander MJ, MacPherson WN, McBride R, et al (2000) Bend measurement using Bragg gratings in multicore fibre. Electronics Letters 36:120–121. https://doi.org/10.1049/el:20000157

6. Park YL, Elayaperumal S, Daniel B, et al (2010) Real-Time Estimation of 3-D Needle Shape and Deflection for MRI-Guided Interventions. IEEE Asme Trans Mechatron 15:906–915. https://doi.org/10.1109/TMECH.2010.2080360

7. Henken K, Van GD, Dankelman J, Van DDJ (2012) Accuracy of needle position measurements using fiber Bragg gratings. Minimally Invasive Therapy 21:408–414. https://doi.org/10.3109/13645706.2012.666251

8. Moore JP, Rogge MD (2012) Shape sensing using multi-core fiber optic cable and parametric curve solutions. Opt Express, OE 20:2967–2973. https://doi.org/10.1364/OE.20.002967

9. Abayazid M, Kemp M, Misra S (2013) 3D flexible needle steering in soft-tissue phantoms using Fiber Bragg Grating sensors. In: 2013 IEEE International Conference on Robotics and Automation. IEEE, pp 5843–5849

10. Roesthuis RJ, Janssen S, Misra S (2013) On using an array of fiber Bragg grating sensors for closed-loop control of flexible minimally invasive surgical instruments. In: 2013 IEEE/RSJ International Conference on Intelligent Robots and Systems. IEEE, Tokyo, pp 2545–2551

11. Borot de BM, Denis de SB, Maenhout M, et al (2016) Fiber Bragg gratings-based sensing for real-time needle tracking during MR-guided brachytherapy. Medical Physics 43:5288–5297. https://doi.org/10.1118/1.4961743

12. Yi X, Chen X, Fan H, et al (2020) Separation method of bending and torsion in shape sensing based on FBG sensors array. Opt Express 28:9367. https://doi.org/10.1364/OE.386738

13. Floris I, Madrigal J, Sales S, et al (2020) Twisting compensation of optical multicore fiber shape sensors for flexible medical instruments. In: Optical Fibers and Sensors for Medical Diagnostics and Treatment Applications XX. International Society for Optics and Photonics, p 1123316

14. Floris I, Madrigal J, Sales S, et al (2020) Twisting measurement and compensation of optical shape sensor based on spun multicore fiber. Mechanical Systems and Signal Processing 140:106700. https://doi.org/10.1016/j.ymssp.2020.106700

15. Jin J, Zhang Y, Zhu Y, et al (2020) Analysis and Correction Method of Axial Strain Error in Multi-Core Fiber Shape Sensing. IEEE Sensors Journal 20:12716–12722. https://doi.org/10.1109/JSEN.2020.3001937

16. Khan F, Donder A, Galvan S, et al (2020) Pose Measurement of Flexible Medical Instruments Using Fiber Bragg Gratings in Multi-Core Fiber. IEEE Sensors Journal 20:10955–10962. https://doi.org/10.1109/JSEN.2020.2993452

17. Megens M, Leistikow MD, van Dusschoten A, et al (2021) Shape accuracy of fiber optic sensing for medical devices characterized in bench experiments. Medical Physics 48:3936–3947. https://doi.org/10.1002/mp.14881

18. Modes V, Ortmaier T, Burgner-Kahrs J (2021) Shape Sensing Based on Longitudinal Strain Measurements Considering Elongation, Bending, and Twisting. IEEE Sensors Journal 21:6712–6723. https://doi.org/10.1109/JSEN.2020.3043999

19. Paloschi D, Bronnikov KA, Korganbayev S, et al (2021) 3D Shape Sensing With Multicore Optical Fibers: Transformation Matrices Versus Frenet-Serret Equations for Real-Time Application. IEEE Sensors Journal 21:4599–4609. https://doi.org/10.1109/JSEN.2020.3032480

20. Lu Y, Lu B, Li B, et al (2021) Robust Three-Dimensional Shape Sensing for Flexible Endoscopic Surgery Using Multi-Core FBG Sensors. IEEE Robotics and Automation Letters 6:4835–4842. https://doi.org/10.1109/LRA.2021.3067279

21. Donder A, Baena FRY (2021) Kalman-Filter-Based, Dynamic 3-D Shape Reconstruction for Steerable Needles With Fiber Bragg Gratings in Multicore Fibers. IEEE Transactions on Robotics 1–14. https://doi.org/10.1109/TRO.2021.3125853

22. Kashyap R (2009) Fiber bragg gratings. Academic press

23. Henken KR, Dankelman J, Dobbelsteen JJVD, et al (2014) Error Analysis of FBG-Based Shape Sensors for Medical Needle Tracking. IEEE/ASME Transactions on Mechatronics 19:1523–1531. https://doi.org/10.1109/TMECH.2013.2287764

24. Mandal KK, Parent F, Kashyap R, et al (2017) Assessment of the Accuracy of Optical Shape Sensing for Needle Tracking Interventions. Journal of Medical Devices-Transactions of the Asme 11:. https://doi.org/10.1115/1.4036338

25. Li M, Li G, Gonenc B, et al (2016) Towards human-controlled, real-time shape sensing based flexible needle steering for MRI-guided percutaneous therapies. Int J Med Robot 13:. https://doi.org/10.1002/rcs.1762

26. Roesthuis RJ, Kemp M, Dobbelsteen JJVD, Misra S (2014) Three-Dimensional Needle Shape Reconstruction Using an Array of Fiber Bragg Grating Sensors. IEEE/ASME Transactions on Mechatronics 19:1115–1126. https://doi.org/10.1109/TMECH.2013.2269836

27. Bronnikov K, Bronnikov K, Wolf A, et al (2019) Durable shape sensor based on FBG array inscribed in polyimide-coated multicore optical fiber. Opt Express, OE 27:38421–38434. https://doi.org/10.1364/OE.380816

28. Khan F, Denasi A, Barrera D, et al (2019) Multi-Core Optical Fibers With Bragg Gratings as Shape Sensor for Flexible Medical Instruments. IEEE Sensors Journal 19:5878–5884. https://doi.org/10.1109/JSEN.2019.2905010

29. Chen X, Yi X, Qian J, et al (2020) Updated shape sensing algorithm for space curves with FBG sensors. Optics and Lasers in Engineering 129:106057. https://doi.org/10.1016/j.optlaseng.2020.106057

30. Rajabzadeh A, Heusdens R, Hendriks RC, Groves RM (2018) Calculation of the Mean Strain of Smooth Non-Uniform Strain Fields Using Conventional FBG Sensors. J Lightwave Technol 36:3716–3725. https://doi.org/10.1109/JLT.2018.2849212

31. Seifabadi R, Gomez EE, Aalamifar F, et al (2013) Real-time tracking of a bevel-tip needle with varying insertion depth: Toward teleoperated MRI-guided needle steering. In: 2013 IEEE/RSJ International Conference on Intelligent Robots and Systems. pp 469–476

32. Cui J, Zhao S, Yang C, Tan J (2018) Parallel Transport Frame for Fiber Shape Sensing. IEEE Photonics Journal 10:1–12. https://doi.org/10.1109/JPHOT.2017.2782736

33. Ourak M, De Buck S, Ha XT, et al (2021) Fusion of Biplane Fluoroscopy with Fiber Bragg Grating for 3D Catheter Shape Reconstruction. IEEE Robotics and Automation Letters 1–1. https://doi.org/10.1109/LRA.2021.3094238

34. Qiao Q, Borghesan G, De Schutter J, Vander Poorten E (2021) Force from Shape—Estimating the Location and Magnitude of the External Force on Flexible Instruments. IEEE Transactions on Robotics 37:1826–1833. https://doi.org/10.1109/TRO.2021.3062504

35. Misra S, Reed KB, Schafer BW, et al (2010) Mechanics of Flexible Needles Robotically Steered through Soft Tissue. The International Journal of Robotics Research 29:1640–1660. https://doi.org/10.1177/0278364910369714

36. Zhang L, Li C, Zhang X, et al (2019) A New Method For Fiber Bragg Grating Based Needle Shape Sensing Calibration. In: 2019 IEEE International Conference on Robotics and Biomimetics (ROBIO). pp 1953–1958

37. Jäckle S, Eixmann T, Schulz-Hildebrandt H, et al (2019) Fiber optical shape sensing of flexible instruments for endovascular navigation. Int J CARS 14:2137–2145. https://doi.org/10.1007/s11548-019-02059-0